Full-Field Near-Field Optical Microscope for Cell Imaging

Thomas Barroca,[1] Karla Balaa,[1,2] Sandrine Lévêque-Fort,[2] and Emmanuel Fort[1]

[1]*Centre d'Imageries Plasmoniques Appliquées, Institut Langevin, Ecole Supérieure de Physique et de Chimie Industrielles (ESPCI) ParisTech, CNRS UMR 7587, Université Paris Diderot, 10 rue Vauquelin, 75231 Paris Cedex 05, France*

[2]*Institut des Sciences Moléculaires d'Orsay and Centre de photonique Biomédicale (CLUPS), Université Paris-Sud 11, CNRS UMR 8214, F91405 Orsay cedex, France*

(Received 5 January 2012; published 22 May 2012)

We report a new full-field fluorescence microscopy method for imaging live cell membranes based on supercritical near-field emission. This technique consists of extracting the self-interference between undercritical and supercritical light by simple image subtraction. In the objective back focal plane, this is equivalent to adding a virtual mask blocking the subcritical emission. We show that this virtual mask is radically different from a real physical mask, enabling a 100 nm axial confinement and enhancing the image sensitivity without damaging the lateral resolution. This technique is easy to implement and simultaneously provides images of the inner parts of the cell and its membrane with standard-illumination light.

DOI: 10.1103/PhysRevLett.108.218101 PACS numbers: 87.64.M−, 87.64.kv

Until recently, it was widely accepted that far-field optical microscopes were limited by diffraction and consequently could not resolve details much finer than about half the wavelength of light. In the last 20 years, a variety of optical methods have been developed to overcome the diffraction limit and achieve nanoscale spatial resolution [1]. In this quest, axial resolution needs to be addressed specifically because of the symmetry of the implementation setups. In addition, improving axial resolution is crucially important for numerous biological applications. For instance, numerous cell mechanisms involve processes occurring at the membrane with only minute concentrations of biomolecules [2]. To track these molecules, it is necessary to remove the background fluorescence from the inner parts of the cell that blur the image and drastically reduce its sensitivity.

The various optical techniques that have been developed to improve the axial confinement can be sorted into either excitation confinement techniques or emission-based techniques. In cell membrane imaging, the favored technique today is total internal reflection fluorescence (TIRF) microscopy based on excitation confinement and obtained through supercritical illumination [3]. The evanescent incident field has a typical sample penetration depth of about 100 nm. However, this technique suffers from both technical and fundamental limitations (loss of confinement due to light scattering, inhomogeneous illumination due to laser coherence, etc.) [4], which have recently triggered developments in its counterpart emission-based geometry called supercritical angle fluorescence (SAF) microscopy [5,6].

SAF microscopy is based on the detection confinement associated with the collection of the fluorophore electromagnetic near-field components. When the fluorophores are in the direct vicinity of the glass interface, these components become propagative and decrease sharply with distance from the interface. In its scanning version, this technique has proven to be very powerful with the ability to perform topography with a nanometer-scale resolution [7]. Nevertheless, this geometry is not adapted for live cell imaging due to the use of a parabolic objective that needs to scan the sample in order to obtain an image. In its full-field version, SAF uses a commercial, high numerical aperture (NA) objective lens. The technique consists of selecting the SAF light by using a mask to block the undercritical angle fluorescence (UAF) components in the back focal plane (BFP) of the objective. Although it also achieves axial sectioning and offers some advantages over TIRF (in particular, laser illumination is unnecessary), this approach has been hampered by a degradation of the image resolution [6,8]. Indeed, the point-spread function (PSF) collecting only the SAF components would result in a significant loss of lateral resolution and a weak contrast in the image. Usually, the emission-based techniques take advantage of the transverse image to store information on the axial position. Hence, techniques such as lens astigmatism [9], double-plane detection [10], off-focus imaging [11], or a double-helix point-spread function [12] are not compatible with direct full-field imaging.

Here, we present an emission-based technique that improves the axial resolution while maintaining the lateral one. This full-field method is based on the subtraction between two images: one image $I_{\mathrm{UAF+SAF}}$ composed of all the emission components (UAF + SAF) and another image I_{UAF} containing only UAF components. This full-field SAF method is therefore designated as virtual SAF (νSAF) because, as it will be shown, it can be interpreted as using a kind of virtual mask that blocks the UAF components in the BFP of the objective.

The first image is directly obtained without any change using a standard epifluorescence microscope equipped with a high NA objective to collect the SAF components. The second image is the result that would be obtained with

an objective of NA equal to the critical angle. The resulting image of νSAF is given by $I_{\nu\mathrm{SAF}} = I_{\mathrm{UAF+SAF}} - I_{\mathrm{UAF}}$, whereas the image of the standard SAF with a real mask is I_{SAF}. To understand the difference between the two images, it is convenient to write the PSF in terms of electric field and separate it into supercritical and undercritical components, respectively denoted E_{SAF} and E_{UAF}. For the sake of clarity, we have removed the vectorial nature of the electric field, the summation over all the emission directions, and the spatial dependence on the image. With a real mask, the SAF PSF is thus simply given by $I_{\mathrm{SAF}} = |E_{\mathrm{SAF}}|^2$. However, the main contribution to the virtual SAF PSF is the interference term (the first order in E_{UAF}):

$$I_{\nu\mathrm{SAF}} = |E_{\mathrm{UAF}} + E_{\mathrm{SAF}}|^2 - |E_{\mathrm{UAF}}|^2 = I_{\mathrm{SAF}} + 2|\mathrm{Re}(E_{\mathrm{UAF}}E^*_{\mathrm{SAF}})| \approx 2|\mathrm{Re}(E_{\mathrm{UAF}}E^*_{\mathrm{SAF}})|. \quad (1)$$

It is important to remember here that although the emission between two fluorophores is incoherent, the emission of a single fluorophore is spatially coherent and its components can consequently interfere with each other. The first term I_{SAF} corresponds to the standard SAF image. The second term $|\mathrm{Re}(E_{\mathrm{UAF}}E^*_{\mathrm{SAF}})|$ is the interference term between the subcritical and supercritical components: this is the dominant term of $I_{\nu\mathrm{SAF}}$. The SAF component is always smaller than the UAF one and decreases sharply with the distance z from the interface while the UAF component remains constant (e.g., $E_{\mathrm{UAF}} \approx 8E_{\mathrm{SAF}}$ at $z = \lambda/15$ for a Cy5 fluorophore: $\lambda = 670$ nm [7]).

We have used the vectorial Debye integral model [13] to simulate the PSF (calculations are performed for a wavelength $\lambda = 593$ nm). Figures 1(a)–1(c) show, respectively, the PSF profile (x axis) as a function of the fluorophore-surface distance z (y axis) in UAF + SAF, UAF, and νSAF. The intensity has been normalized at $z = 0$. As expected, the intensity collected in Fig. 1(b) is less important than in Fig. 1(a) since the collection efficiency has been reduced when collecting only the UAF components. Figure 1(c) is the result of the subtraction of the two previous images. It shows that the intensity decreases sharply with distance z, allowing the axial sectioning needed for cell membrane imaging. The axial profile can be well fitted with an exponential, as in the case of SAF and TIRF, and provides similar penetration depth values [Fig. 1(c)]. Moreover, the changes on the PSF profile with distance z are minimal. To compare the lateral resolution, we have plotted the PSF profile of the different components for a fluorophore at the surface ($z = 0$) in Fig. 1(d). The PSF profile for an image collecting only the UAF components is slightly larger than the epifluorescence image (UAF + SAF) since the NA of the objective is reduced. However, the subtraction between those two profiles gives a better PSF. Hence, the νSAF technique leads to axial confinement that also conserves a high lateral resolution in full field. This result contrasts with the standard SAF technique [Fig. 1(d)]. In this latter case, the extension of

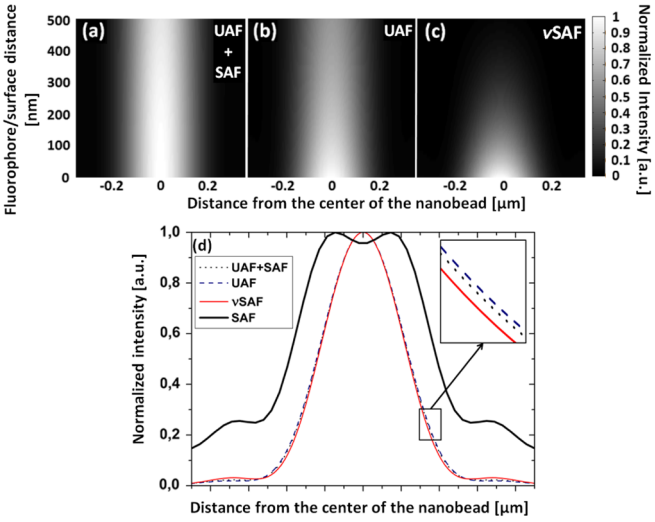

FIG. 1 (color online). PSF profile as a function of the fluorophore-surface distance z for (a) UAF + SAF, (b) UAF, and (c) νSAF. The intensity of the signal is normalized at $z = 0$. (d) shows the theoretical PSF profiles in UAF + SAF, UAF, νSAF and SAF for 100 nm beads deposited at the surface. The νSAF technique conserves the lateral resolution.

the PSF is given by the Fourier transform of the SAF circle in the BFP and strongly depends on the width of this circle [8]. We have also used the vectorial Debye model to evaluate the contrast of the technique. The PSF profiles of two 100 nm beads deposited at the surface and spaced by a distance d have been simulated [Fig. 2(a)]. The normalized contrast C is then given by

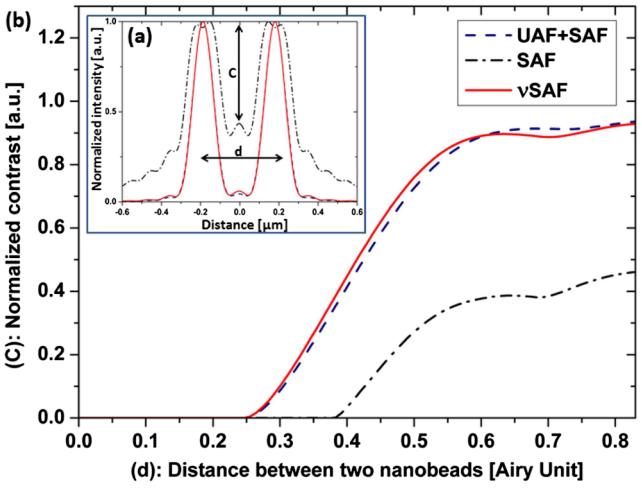

FIG. 2 (color online). (a) Normalized PSF profiles in UAF + SAF, SAF, and νSAF for two nanobeads spaced by a distance d. (b) Normalized contrast in UAF + SAF, SAF, and νSAF. The larger PSF in the SAF technique leads to a weak contrast. The νSAF technique allows us to recover a better contrast comparable to that of the standard epifluorescence image (UAF + SAF).

$$C = \frac{I_{\max} - I_{\min}}{I_{\max} + I_{\min}}, \quad (2)$$

where $I_{\max}$ and $I_{\min}$ are, respectively, the maximum and minimum intensities of the signal. Figure 2(b) shows the normalized contrast in UAF + SAF, SAF, and νSAF. We observe a better contrast in the νSAF technique: at a half Airy unit, the contrast is 2.7 times higher in νSAF than in SAF. The larger PSF in the SAF technique leads to a weak contrast while the better lateral resolution of the νSAF technique allows us to obtain a contrast comparable to that of the standard epifluorescence image (UAF + SAF).

The νSAF technique has been implemented with the setup shown in Fig. 3. It is composed of a commercial inverted microscope (Nikon Ti) with an apochromatic objective lens (1.49 NA 60× from Nikon), an EM-CCD camera (iXon+ from Andor Technology), and a standard fibered 130 W mercury lamp combined with a cube filter to select the excitation and emission wavelengths. The νSAF optical system is mounted between the microscope and the camera. It comprises three lenses: $L2$ and $L3$, respectively (with focal lengths $f_2 = f_3 = 100$ mm), form the BFP of the objective in the νSAF module and the image plane (IP) on the camera; and a removable Bertrand lens BL ($f_{\mathrm{BL}} =$ 75 mm) to image the BFP on the camera. To realize the subtraction between two images (one with all the light components $I_{\mathrm{UAF+SAF}}$ and the other with only the UAF components I_{UAF}), a fast filter wheel from Thorlabs has been put into the conjugate plane of the BFP. It allows a fast switch (in less than 50 ms) between the UAF+SAF image [Fig. 3(a)] and the UAF image [Fig. 3(b)]. The positioning of the wheel is performed with an XY micrometric translation stage. The result of the subtraction between the two previous images [Fig. 3(c)] is equivalent to a virtual mask where only the SAF components are conserved. The corresponding images in the IP (with exposure time 100 ms) are shown in Figs. 3(d)–3(f) for an N2a mouse neuroblastoma cell tagged with mCherry. Figures 3(d) and 3(e) are almost identical, since little of the signal has been removed. However, the subtraction of those two images (pixel-to-pixel subtraction) reveals the cell membrane [Fig. 3(f)]. The entire image acquisition process is controlled by LABVIEW interface. It is noteworthy that, contrary to TIRF, the optical setting is very easy and there is no need for a laser source. Hence, a simple incoherent white light will provide a much better homogeneous illumination field. Besides, the acquisition rate of νSAF images is that of the total acquisition rate since it is possible to obtain an image from any set of two successive images (with and without SAF components) regardless of the acquisition order. At the same rate, it is possible to obtain simultaneously the standard epifluorescence image of the cells since the UAF image is very similar to the UAF + SAF image. This information related to the inner cell activity is of particular interest in many applications.

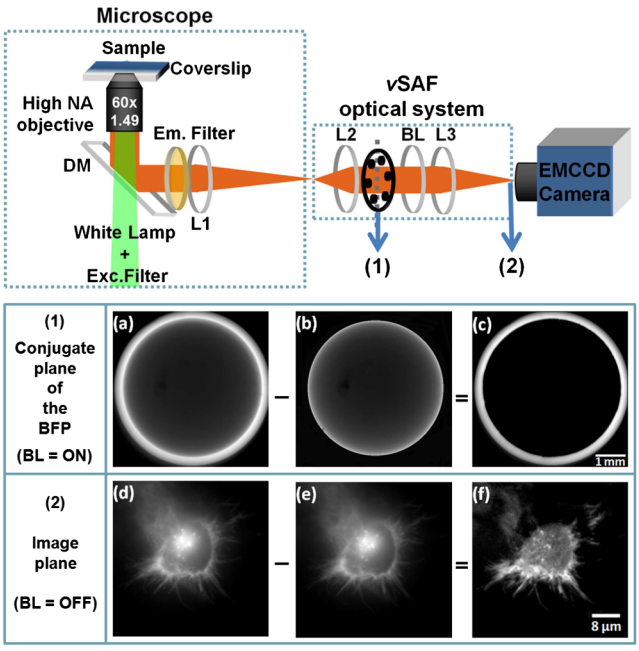

FIG. 3 (color online). Experimental setup. A standard fluorescent microscope equipped with a white lamp, a large NA objective lens (1.49), and an EM-CCD camera are used. The νSAF optical system is mounted between the microscope and the camera. A filter wheel has been synchronized with the camera to take one image with the whole BFP (a) and a second with only the UAF components (b)–(c) is the result of the subtraction (a)–(b) to obtain the virtual mask where only the SAF components are conserved. (d)–(f) show the corresponding images of an N2a cell in the image plane.

We have used 100 nm fluorescent latex beads (FluoSpheres® carboxylate-modified microspheres from Life Technologies) deposited at the surface to measure the PSFs experimentally. Figures 4(a)–4(c) show, respectively, a bead in UAF + SAF, νSAF, and SAF in the IP magnified 6.7 × . The PSF profile of each mode has been plotted. We noticed a νSAF profile that is slightly larger than expected. This limitation probably originates from the aberrations of the high NA objective. (Their tuning is of crucial importance.) However, the νSAF profile is equivalent to that of UAF + SAF and greatly improves the lateral resolution as compared to the standard SAF technique.

We have also compared the νSAF technique on biological samples. First, the comparison has been done with the standard SAF technique. In this experiment, the filter wheel has been programmed to take three different components in the BFP: UAF + SAF, UAF, and SAF. The first two images are used to obtain the images in epifluorescence and νSAF. The third one allows us to obtain the standard SAF image. Human embryonic kidney (HEK 293) cells transfected with type I cannabinoid receptors tagged with green fluorescent protein (CB1R-GFP) have been used. Figures 5(a)–5(c), respectively, show HEK in

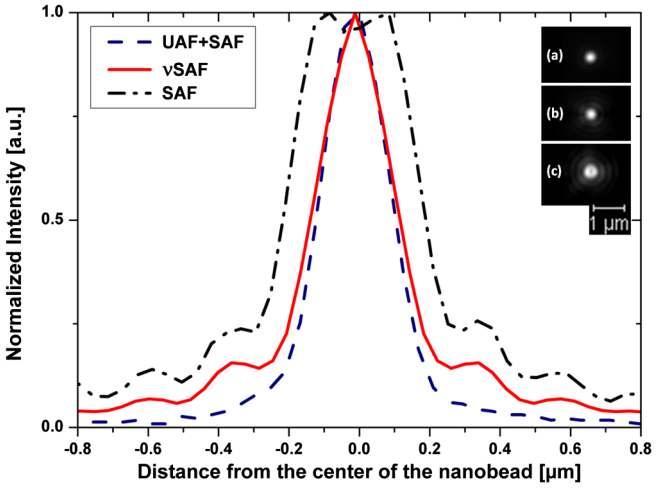

FIG. 4 (color online). A 100 nm fluorescent latex bead in (a) epifluorescence (UAF + SAF), (b) νSAF and (c) SAF. The bead profiles from those three images have been plotted. The improvement of the lateral resolution with the νSAF is significant.

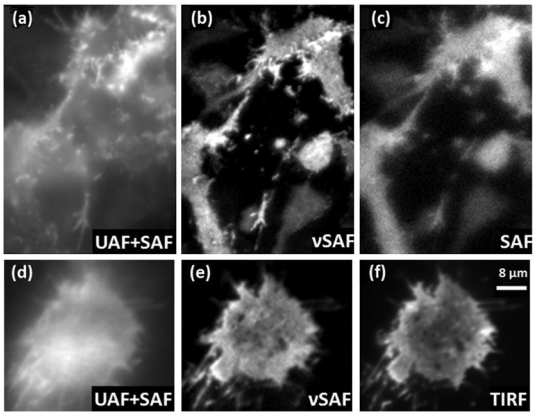

FIG. 5. HEK cell tagged with GFP in (a) UAF + SAF, (b) νSAF and (c) SAF. The improvement in lateral resolution and contrast is significant in the νSAF image. N2a mouse neuroblastoma cell tagged with mCherry in (d) UAF + SAF, (e) νSAF and (f) TIRF. The νSAF image is comparable to the TIRF image in terms of lateral resolution and axial sectioning.

UAF + SAF, νSAF and SAF. Those images confirm that membranes appear with a higher contrast and a better lateral resolution with the νSAF method. Then, we have compared νSAF with the most common technique based on excitation confinement: the TIRF technique. N2a mouse neuroblastoma cells tagged with mCherry have been used for this purpose. Exceptionally, the white lamp has been replaced by a green laser ($\lambda = 532$ nm) to switch from an epi-illumination to a TIRF-illumination. Figures 5(d) and 5(e), respectively, show the UAF + SAF and νSAF images. For comparison, the image obtained with a TIRF-illumination is shown in Fig. 5(f). This result shows that the νSAF technique allows cell membrane imaging comparable to the TIRF in terms of lateral resolution and confinement. Moreover, it is important to note that the νSAF image is obtained in epi-illumination, which enables the simultaneous observation of Figs. 5(d) and 5(e), while the TIRF technique requires a change in the angle of illumination.

In this Letter, we have introduced a new, powerful full-field method in live cell microscopy based on PSF engineering and self-interference. This method is particularly well suited for real-time imaging of membrane processes. Since the image is obtained in epi-illumination, this technique allows us to follow the cell shape and its membrane simultaneously, which is of particular interest in many applications. Contrary to the standard technique to obtain a full-field SAF image, νSAF offers no loss of lateral resolution and a higher contrast. Contrary to TIRF, there is no need for laser sources and complex excitation, which allows a homogeneous illumination of the sample and therefore a constant axial sectioning over all of the IP. We are currently combining νSAF with other microscopy techniques in the context of biomedical issues.

The authors thank C. Boccara and S. Grésillon for fruitful discussions, A. Roland and S. Lécart for cell samples, and F. Quinlan-Pluck for helpful comments on this Letter. This work has been supported by grants from Region Ile de France, C'Nano Ile de France, and the Triangle de la Physique.

[1] S. W. Hell, Nat. Methods **6**, 24 (2009).
[2] M. S. Bretscher and C. Aguado-Velasco, Curr. Opin. Cell Biol. **10**, 537 (1998).
[3] D. Axelrod, Traffic **2**, 764 (2001).
[4] E. Fort and S. Grésillon, J. Phys. D **41**, 013001 (2008).
[5] T. Ruckstuhl, J. Enderlein, S. Jung, and S. Seeger, Anal. Chem. **72**, 2117 (2000).
[6] D. Axelrod, J Biomed. Opt. **6**, 6 (2001).
[7] C. M. Winterflood, T. Ruckstuhl, D. Verdes, and S. Seeger, Phys. Rev. Lett. **105**, 108103 (2010).
[8] T. Barroca, K. Balaa, J. Delahaye, S. Lévêque-Fort, and E. Fort, Opt. Lett. **36**, 3051 (2011).
[9] B. Huang, W. Wang, M. Bates, and X. Zhuang, Science **319**, 810 (2008).
[10] M. F. Juette, T. J. Gould, M. D. Lessard, M. J. Mlodzianoski, B. S. Nagpure, B. T. Bennett, S. T. Hess, and J. Bewersdorf, Nat. Methods **5**, 527 (2008).
[11] M. Speidel, A. Jonás, and E.-L. Florin, Opt. Lett. **28**, 69 (2003).
[12] S. R. P. Pavani, M. A. Thompson, J. S. Biteen, S. J. Lord, N. Liu, R. J. Twieg, R. Piestun, and W. E. Moerner, Proc. Natl. Acad. Sci. U.S.A. **106**, 2995 (2009).
[13] W. T. Tang, E. Chung, Y-H Kim, P. T. C. So, and C. J. R. Sheppard, Opt. Express **15**, 4634 (2007).